Microfluid Nanofluid (2009) 7:307–323
DOI 10.1007/s10404-008-0375-4

RESEARCH PAPER

Simulation of advanced microfluidic systems with dissipative particle dynamics

Thomas Steiner · Claudio Cupelli · Roland Zengerle · Mark Santer

Received: 8 October 2008 / Accepted: 11 November 2008 / Published online: 9 January 2009

Abstract Computational Fluid Dynamics (*CFD*) is widely and successfully used in standard design processes for microfluidic μ*TAS* devices. But for an increasing number of advanced applications involving the dynamics of small groups of beads, blood cells or biopolymers in microcapillaries or sorting devices, novel simulation techniques are called for. Representing moving rigid or flexible extended dispersed objects poses serious difficulties for traditional *CFD* schemes. Meshless, particle-based simulation approaches, such as *Dissipative Particle Dynamics* (*DPD*) are suited for addressing these complicated flow problems with sufficient numerical efficiency. Objects can conveniently be represented as compound objects embedded seamlessly within an explicit model for the solvent. However, the application of *DPD* and related methods to realistic problems, in particular the design of microfluidics systems, is not well developed in general. With this work, we demonstrate how the method appears when used in practice, in the process of designing and simulating a specific microfluidic device, a microfluidic chamber representing a prototypical bead-based immunoassay developed in our laboratory (Glatzel et al. 2006a, b; Riegger et al. 2006).

Thomas Steiner: born Glatzel.

T. Steiner · C. Cupelli · R. Zengerle · M. Santer
Department of Microsystems Engineering IMTEK, University of Freiburg, Georges-Köhler-Allee 106, 79110 Freiburg, Germany

M. Santer (✉)
Fraunhofer Institute for Mechanics of Materials-IWM, Wöhlerstrasse 9, 79108 Freiburg, Germany
e-mail: mark.santer@iwm.fraunhofer.de

Keywords Dissipative particle dynamics · Simulation of microfluidic systems · Lab on a chip

1 Introduction

One of the main objectives of *life science*, a discipline comprising fields as diverse as environmental technology, biochemistry, pharmacology and medical diagnostics, is an attempt to transfer fundamental research results to commercial applications and products. One of the fastest growing fields in this area is the development of so called *Lab-On-A-Chip* devices, or with special emphasis on diagnostics applications, *Micro-Total-Analysis Systems* (μ*TAS*) (Vilkner et al. 2004; Oosterbroek and van den Berg 2003; Haeberle and Zengerle 2007; Harrison et al. 2000; Ducrée and Zengerle 2004; Reyes et al. 2002; Auroux et al. 2002). Their virtues are miniaturization and integration of several chemical or biochemical analysis steps with various microfluidic tasks to process or transport reagents. In medical diagnostics, several μ*TAS* have been developed so far, e.g., to enhance the screening of cardiovascular drugs (Li et al. 2003), to simultaneous detect cardiac risk factors (Kurita et al. 2006; Christodoulides et al. 2002) or to monitor in vivo the glucose and lactate concentration (Kurita et al. 2002, 2006) as well as a wide variety of immunoassays (Sato and Kitamori 2004; Yakovleva et al. 2002, 2003a, b). In a way similar to applying finite-element or electronic-circuit simulation tools for the design of *MEMS*, *CFD*-simulations have become an indispensable tool in the development process of these microfluidic devices. They guarantee reliable designs and help reduce costs during the development phase.

μ*TAS* may involve quite complex mixtures of biological liquids such as emulsions (Haeberle et al. 2007; Hardt and

Schönfeld 2003; Hessel et al. 2003) and cell suspensions (MacDonald et al. 2003; Tabuchi et al. 2004), in combination with added objects such as functionalized colloids or microbeads (Sugiura et al. 2005; Lettieri et al. 2003; Kerby et al. 2002; Sohn et al. 2005). With an increasing number of devices one attempts to manipulate these complex fluids in a controlled manner—examples are bead-based micromixers and immunoassays (Riegger et al. 2006; Grumann et al. 2005; Sato et al. 2002; Saleh and Sohn 2003; Roos and Skinner 2003), cell sorting or *DNA*-separation devices (Yoshida et al. 2003; Wolff et al. 2003; Dittrich and Schwille 2003; Tian et al. 2000; Tian and Landers 2002; Sanders et al. 2003; Doyle et al. 2002; Duong et al. 2003). In these systems, one is dealing with rather complex situations of fluid flow. On the one hand, the number and shape of dispersed objects is so large that their extent and mutual interaction cannot be neglected. On the other hand, they are too few to be described effectively as a rheological fluid with properties that can be parametrized. Additionally, as in the case of emulsions or blood cells, the elastic flexibility of an object has to be taken into account. Because of the great difficulties in generating adaptive and time-dependent meshes, it is impractical for finite-volume schemes to deal with this situation in great generality.

During the last 15 years, various new meshless and particle-based simulation approaches have received considerable attention that can offer solutions to the above-mentioned flow problems (Heyes et al. 2004). Among them are, most notably, recent developments in *Smoothed Particle Hydrodynamics* (*SPH*) (Monaghan 1992), *Lattice gas methods* (*LGM*) (Frisch et al. 1986) and *Dissipative Particle Dynamics* (*DPD*). *LGM* such as the Lattice-Boltzmann-Method implement a pseudo-molecular collision dynamics on a grid in order to emulate the dynamical properties of the Boltzmann equation. Thus, this elegant scheme becomes a very powerful solver for fluid dynamics problems, including even turbulence. Phenomena such as multi-phase flows (Sbragaglia et al. 2007) have been implemented, and studies addressing complete microfluidic systems have recently been presented (Dupin et al. 2006).

The particle-based schemes that employ the solution of Newton's equation of motion to represent the system dynamics seems conceptually simpler. *SPH*, for instance, is actually an alternative discretization of the Navier–Stokes-Equations (NSE), where the grid points represent fluid elements that are co-moving with the local flow field in a Lagrangian frame (Monaghan 2005). With each point, a smooth kernel function is associated. The superposition of kernels permits the evaluation of densities, velocities and their derivatives at other points. The kernel functions lead to effective forces between neighboring points—the initial configuration of points can undergo a substantial redistribution in space, establishing the picture of small interacting amounts of liquid. In advanced schemes such as Smoothed-Dissipative-Particle Dynamics (*SDPD*) the analogy with a small thermodynamic system can be established by incorporating thermal fluctuations (Espanol and Revenga 2003).

DPD, in contrast, was originally proposed in a purely heuristic manner (Hoogerbrugge and Koelman 1992), as an explicit model for solvents and liquid flow on mesoscopic scales. The novel idea was to combine soft repelling forces of generic pseudo-molecules (supposed to represent lumps of fluid) with a *momentum-conserving* thermostat to retain hydrodynamics, while at the same time providing thermal motion. This method was soon put on firm grounds and improved by various authors (Lowe 1999; Masters and Warren 1999; Trofimov 2003; Espanol and Warren 1995), and must properly be viewed as providing a generic model liquid. Technically, the scheme is quite similar to molecular dynamics (MD) simulations—all properties of the model liquid are completely specified by the given inter-particle interactions, which usually are kept advantageous numerically—the integration time step in *DPD* can be chosen at least two orders of magnitude larger than in MD (Groot and Warren 1997).

In the same spirit, one also may build structured objects out of dissipative particles directly. The dynamics of single polymer coils or polymer mixtures can be represented quite faithfully by establishing linear or branched chains of particles that are linked by harmonic forces (Groot and Madden 1998). Solid boundaries or dispersed solid objects may be defined by "freezing" the absolute or relative motion of the constituting particles. This conceptual simplicity renders the method very attractive for addressing general problems in fluid dynamics that are hard to represent or simulate otherwise, irrespective of a particular length or time scale. The rheology of suspensions of rigid, arbitrarily-shaped objects has been studied quite successfully (Koelman and Hoogerbrugge 1993; Boek et al. 1997; Pryamitsyn and Ganesan 2005), but also purely hydrodynamic problems have been addressed—in studying flow around periodic arrays of cylinders the *DPD* simulation was shown to resolve even fine details of asymptotic corrections to the flow field (Keaveny et al. 2005).

On the other hand, the majority of previous studies with *DPD* and related methods have mostly been applied in idealized situations in a rather generic manner. Many aspects important for carrying out studies for specific microfluidic systems are not yet well developed. In this work, we explore the *DPD* approach with respect to representing a realistic engineering problem involving the design process of a special type of a microfluidic chamber serving as a bead-based immunoassay. In this chamber, microspheres with immobilized capture proteins are supposed to aggregate in as regular a pattern as possible to facilitate fluorescent readout (Riegger et al. 2006), see also

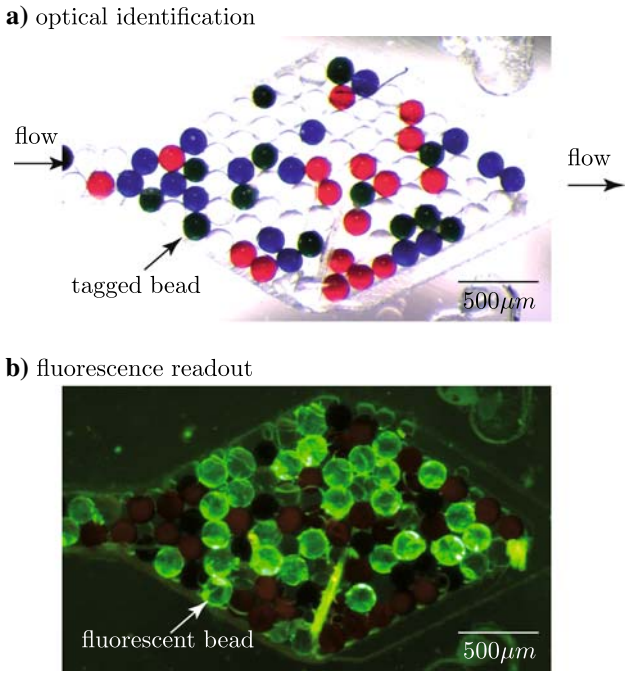

Fig. 1 Typical read-out procedure for multiplexed bead-based immunoassays as studied previously by the authors (Riegger et al. 2006). **a** First, the tagged beads are optically identified by their color. **b** Second, the fluorescent intensity is measured for each optical tag (color online)

Fig. 1. Prerequisites for a regular and reproducible aggregation pattern are a careful design of flow geometry, the shape of the chamber and the interactions of the microspheres (Roos and Skinner 2003; Stone et al. 2004). On the way to a time-dependent simulation of the aggregation process in comparison to experiments, we illustrate a possible validation process, which will indeed reveal the limitations but especially the virtues of the simulation approach.

This work is organized as follows. In the following section, we outline the fundamentals of the *DPD* approach. Subsequently we discuss the role a *DPD* simulation can play in a design process of a μ*TAS* application. In some detail, we explain the quaternion approach to representing compound rigid objects, since it is a very efficient and elegant method to propagate objects of arbitrary shape, but does not appear to be widely used. Finally, we compare the process of successive aggregation of microspheres to experimental results.

2 Fundamentals of dissipative particle dynamics

In *DPD*, fluids and soft matter are modeled by pairwise interacting particles [which we shall in general refer to as fluid particles (*FP*)], the dynamics of which follows Newton's second law

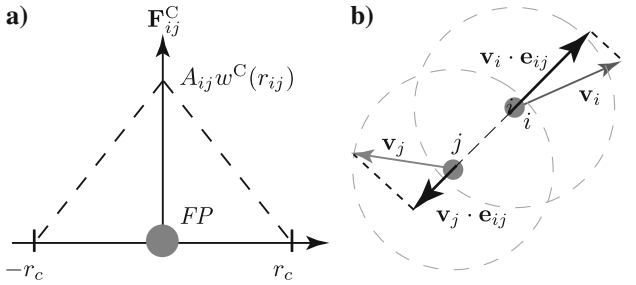

Fig. 2 **a** Pair-force of a fluid particle. **b** Calculation of the relative velocity $\mathbf{v}_{ij}$ between two particles

$$\mathbf{F}_i = m_i \ddot{\mathbf{r}}_i, \tag{1}$$

with the mass m_i of particle i and its spatial coordinate $\mathbf{r}_i$ in the laboratory-fixed frame. $\mathbf{F}_i$ is the total force acting on it. In the simplest form, $\mathbf{F}_i$ is the sum of pairwise conservative, dissipative and random forces,

$$\mathbf{F}_i = \sum_j \left(\mathbf{F}^{\mathrm{C}}_{ij} + \mathbf{F}^{\mathrm{D}}_{ij} + \mathbf{F}^{\mathrm{R}}_{ij}\right) + \mathbf{F}^{\mathrm{ext}}_i, \tag{2}$$

$\mathbf{F}^{\mathrm{ext}}_i$ is an external force such as gravity. The conservative force in standard *DPD* is a soft central repulsion acting between particle i and j:

$$\mathbf{F}^{\mathrm{C}}_{ij} = \begin{cases} A_{ij} w^{\mathrm{C}}(r_{ij}) \mathbf{e}_{ij} & r_{ij} < 1 \\ 0 & r_{ij} \geq 1, \end{cases} \tag{3}$$

where $\mathbf{r}_{ij} = \mathbf{r}_i - \mathbf{r}_j$, $r_{ij} = |\mathbf{r}_{ij}|$ and $\mathbf{e}_{ij} = \mathbf{r}_{ij}/r_{ij}$. The weight function $w^{\mathrm{C}}(r) = (1 - r/r_c)$ vanishes for an inter-particle distance r larger than a cutoff radius r_c (cf Fig. 2a), and determines the effective range of forces. r_c is conveniently taken as the unit of length, and is usually set to unity ($r_c = 1$). A soft potential allows to choose a large time step in general, but would give rise to a very low viscosity. In fact, if the conservative force is sufficiently weak, the major part of the viscosity is provided by the dissipative force $\mathbf{F}^{\mathrm{D}}_{ij}$ (Groot and Warren 1997),

$$\mathbf{F}^{\mathrm{D}}_{ij} = \begin{cases} -\gamma \omega^D(r_{ij})(\mathbf{v}_{ij} \cdot \mathbf{e}_{ij}) \mathbf{e}_{ij} & r_{ij} < 1 \\ 0 & r_{ij} \geq 1, \end{cases} \tag{4}$$

with contributions from the random force $\mathbf{F}^{\mathrm{R}}_{ij}$ (Marsh et al. 1997),

$$\mathbf{F}^{\mathrm{R}}_{ij} = \begin{cases} \sigma w^{\mathrm{R}}(r_{ij}) \xi_{ij} \mathbf{r}_{ij} (\Delta t)^{\frac{1}{2}} & r_{ij} < 1 \\ 0 & r_{ij} \geq 1, \end{cases} \tag{5}$$

where σ is the amplitude of the random variable ξ_{ij}. The dissipative force is proportional to the relative velocity $\mathbf{v}_{ij} = \mathbf{v}_i - \mathbf{v}_j$ of two *FP*s, as illustrated in Fig. 2b). Note the dependence of $\mathbf{F}^{\mathrm{R}}$ on the square root of the integration time step Δt: $\mathbf{F}^{\mathrm{D}}_{ij}$ and $\mathbf{F}^{\mathrm{R}}_{ij}$ obey a fluctuation–dissipation theorem where σ and γ are related by $\sigma^2 = 2\gamma k_{\mathrm{B}} T$ and $w^{\mathrm{R}}_{ij}(r)^2 = w^{\mathrm{D}}_{ij}(r)$, k_B is the Boltzmann constant. Together they act as a thermostat keeping the system at a defined temperature T.

The usual choice for the weight functions is $w^R = w^C$ (Espanol and Warren 1995). In this work, Eq. 1 is solved with a *Velocity-Verlet* algorithm put forward by Groot and Warren (1997) and described in Appendix B.1. Improved versions of the thermostat (Lowe 1999; Peters 2004) have been suggested to eliminate time step effects of the simple Velocity-Verlet scheme (Vattulainen et al. 2002).

The forces introduced above are central, and imply conservation of linear and angular momentum. Espanol (1995) finally showed that if sufficient spatio-temporal averages of velocities $\bar{\mathbf{v}}$ and densities $\bar{\rho}$ are considered, the NSE are obeyed with a well defined viscosity $\bar{\eta}$,

$$\bar{\rho}\frac{\partial}{\partial t}\bar{\mathbf{v}} + \bar{\rho}\bar{\mathbf{v}}\cdot\nabla\bar{\mathbf{v}} = -\nabla p + \bar{\eta}\nabla^2\bar{\mathbf{v}} + \bar{\rho}\mathbf{g}, \tag{6}$$

p is the pressure distribution and $\mathbf{g}$, a body force. For the simple force law (3) the equation of state (EOS) reads

$$p = \bar{\rho}k_BT + \alpha A\bar{\rho}^2, \tag{7}$$

where α is a correction factor arising from a mean-field approximation (Groot and Warren 1997). Many extensions of the simple scheme above have been proposed, such as additional internal degrees of freedom (Espanol 1998), or tailor-made equations of state, including cohesive properties (Pagonabarraga and Frenkel 2001); Eq. 7 does not yet provide a Van-der-Waals loop that would allow for the coexistence of a vapor and a liquid phase.

Two comments are in order. First, with a chosen set of model quantities (e.g., A, T and γ) there is, in general, no simple relation to transport parameters such as diffusivities and viscosities; these must, strictly speaking, be determined by methods of statistical mechanics (Ripoll et al. 2001). In practice, however, this is rarely necessary, as these properties are easily measured numerically for sufficiently many reference points in parameter space by standard methods of non-equilibrium *MD* (Allen and Tildesley 1987). In our work, we have used Lees-Edwards boundary conditions in order to obtain the viscosity measured at a spatially homogeneous shear rate. For vanishing A, our results agree with the simple analytical estimate put forward in Groot and Warren (1997). However, increasing the interparticle repulsion to $A = 250$ (at $\sigma = 5$, $k_BT = 1$ and $\rho = 5$ will increase $\bar{\eta}$ by roughly a factor of 6). Second, as long as generic force laws are used, the EOS of the model liquid will differ significantly from that of real liquid. Thus, there is no immediate relation to a particular time or length scale. Although a restricted mapping of scales is possible for genuine nanoscale applications, exploiting the stochastic character (Groot and Rabone 2001), for a general flow problem this would be rather inconvenient. For instance, representing the relatively high compressibility of a liquid on the scale of the simulation box would require fairly strong repelling forces; but increasing $\mathbf{F}^C$ indefinitely not only increases the viscosity (and thus the integration time step), but ultimately can cause the model liquid to freeze (Trofimov 2003).

In practice, one would instead allow for a rather low compressibility and check that the maximum *Mach number* is sufficiently small. In fact, employing a set of relevant dimensionless quantities to relate the simulation to the real problem on the one hand, and characterizing the limits of the model by another suitable set is the most natural (and useful) way to proceed, as will be outlined in the following section.

3 From design to simulation

3.1 Scope of the DPD modeling

Figure 3 illustrates the overall design of the aggregation chamber. Beads enter the aggregation chamber successively via a thin connecting channel preventing arrival in lumps which could lead to badly-shaped aggregates. The figure also indicates how a rapid-prototyping process for structure optimization would eventually be organized—the CAD-design of the structure serves for constructing both, a discretization mesh as input to a *CFD*-simulation and for defining the location of immobile fluid particles constituting

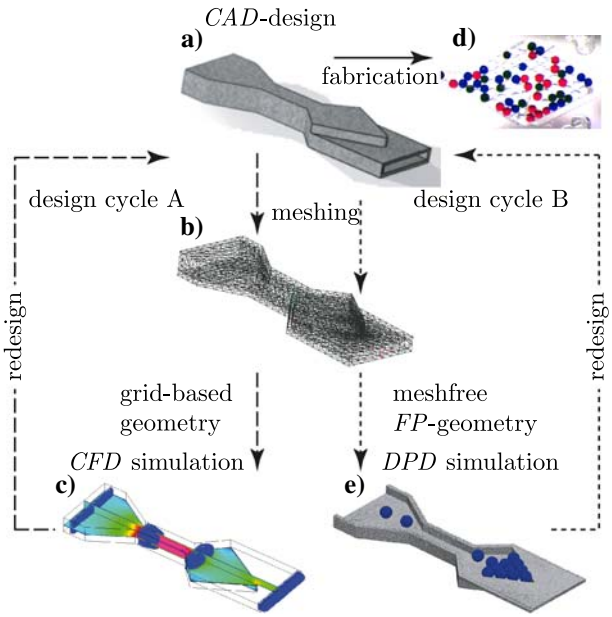

Fig. 3 Workflow from construction to simulation and fabrication of μ*TAS* devices. **a** CAD-Design, turned upside-down (the wall where beads can aggregate (**d**) is shown to the top for better visibility). From the CAD-data, a mesh of grid points can be generated (**b**) that serves both, as discretization for a *CFD*-simulation (**c**) and (with an adapted distribution of grid points) as the positions for solid fluid particles in the *DPD* simulation (**e**) (color online)

the solid boundaries in the *DPD*-simulation (employing an XYZ-format of the CAD-file). In a preliminary design cycle (A), *CFD*-simulations would be used to quickly assess and optimize the overall flow properties of the device, possibly including the connecting peripheral fluidic components. In a subsequent cycle (B), a detailed analysis including the explicit dynamics of several aggregating microspheres is left to the *DPD* simulation, which must then be restricted to the reduced structure actually shown in the figure.

Naturally the question arises, whether the *DPD* scheme and *CFD* may be coupled directly, e.g., by matching stresses and mass flows across suitably chosen interfaces (inlet and outlet). But since *DPD* is a statistical mechanical representation of a liquid, conceptual difficulties as met in a multi-scale coupling of *MD* and continuum descriptions may arise (De Fabritiis et al. 2006), but also technical problems such as numerical instabilities emerge with defining suitable time averages of pressure fields fed back to the *CFD*-solver (see discussion in Sect. 3.3 with respect to the inverse problem). But even if an efficient coupling is found, the *DPD* part will then be the bottleneck of the hybrid scheme. Thus, instead of seeking a direct numerical coupling of *DPD* and *CFD* we suggest that an iterative but seperate scheme as illustrated in Fig. 3 may be simpler to implement in many cases.

In general then, for the *DPD* system, some process of reduction must be carried out, since there is little room for coarsening (such as an adaptive meshing in *CFD*)—as the liquid is represented by a thermodynamic particle ensemble, the EOS dictates that the particle density of the liquid must be the same everywhere. The connecting as well as the inlet channel have been shortened in order to reduce the structure as much as possible without changing its hydrodynamic characteristics. A detailed view is shown in Fig. 4, where the dimensions of the prototype (a) are compared to those used in the *DPD* simulation (b). One usually can make other admissible simplifications of the experimental situation. As the connecting channel effectively injects single microspheres into the aggregation chamber at a time, this inflow of beads can be emulated in the simulation by a generic source

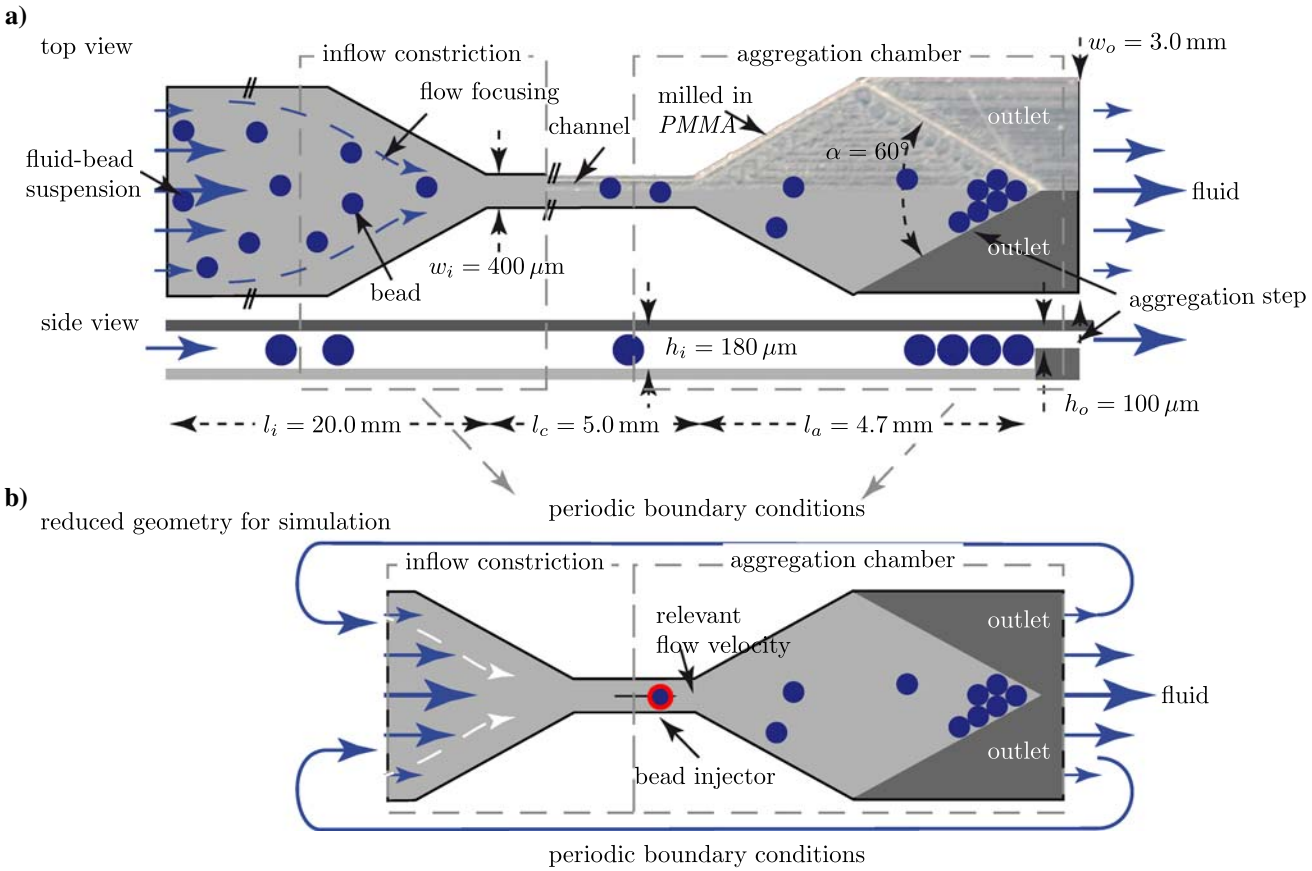

Fig. 4 Diamond-shaped microfluidic aggregation chamber with inlet at the left and outlet at the right side. Suspended polystyrene beads of diameter $d_B = 150$ μm enter the inlet during the experiments at the left. **a** Geometry of experiments: the inflow constriction, channel and aggregation chamber are $h_i = 180$ μm in height, while the outlet height is set to $h_o = 100$ μm. **b** Reduced simulation model: flow boundary conditions are realized with periodic boundary conditions in *DPD* and not with coupled *CFD* simulation with beads introduced at the bead injector (color online)

of beads placed at a certain distance away from the inflow expansion. This source is termed *bead injector* and its location is indicated in Fig. 4b. The application of correct boundary conditions (pressure and/or velocity) can then be simplified by applying periodic boundary conditions—if inlet and outlet channel are given the same rectangular cross sections, *FP*s leaving the outlet can immediately be made re-enter through the inlet (microspheres leaving through the outlet can be removed "on the fly" by removing the constraints between their constituting *FP*s, see also Sect. 4). Here we have to make sure that the opening of the inflow constriction is chosen such that the expected flow profile at the outlet is not affected. An additional overhead of fluid particles is, in general, required to model the solid boundaries of the device. Although there are prescriptions to represent flat or smooth walls by structureless interfaces where suitable reflection rules ensure well-defined flow boundary conditions [e.g., *no slip* (Revenga et al. 1999)], for complicated geometries as shown in Fig. 3 this procedure becomes increasingly cumbersome. It is therefore almost inevitable to model the chamber walls explicitly, e.g., as frozen arrangements of fluid particles. Technically this is very simple and as mentioned above, a mesh tool may conveniently be used to define the geometry and subsequently adapt quickly to an optimal particle distribution. Except for being immobile, the particles making up the solid (s) interact with the ones of the liquid (l) over the same force law (2). This is convenient since properties such as contact angles can be realized by defining different relative interactions strengths A_{ij} between different species of particles (Clark et al. 2000; Kong and Yang 2006). In our case we distinguish between particles defining the solid boundaries (s), the liquid (l), and "beads" (b), with relative force constants A_{sl}, A_{sb} and A_{bl}. This way it is a simple matter to render walls or microspheres hydrophilic or hydrophobic, for instance.

Tuning physical properties by adjusting inter-particle forces appears very convenient on the one hand. On the other, technical artifacts are likely to occur. The solid–liquid interface is an example—it may become diffuse or even leakage of fluid occurs if repelling forces are chosen too soft. To make boundaries impenetrable, one must either increase the density of *FP* within the wall or choose a larger relative repulsion strength. These simple remedies may occasionally lead to undesired slip (Pivkin and Karniadakis 2006), particle layering and thus significant density oscillations near flat walls (Revenga et al. 1998), see also Fig. 6. The solid–liquid interface probes the resolution limit of the particle scheme, and care is required in cases like this. We have shown (Henrich et al. 2007) [using a many-body force law (Warren 2003)] that a smooth density profile without leakage can be achieved if only a rather thin diffuse interface and negligible slip is allowed for. In practice, we find that limitations as discussed above play a minor role in representing hydrodynamic features adequately if only the size of the model system is chosen sufficiently large. Simulation and experiment can then be matched by comparing a suitable set of dimensionless quantities, as outlined in the following. This will later be contrasted with the process of aggregation, where microspheres interact mechanically.

3.2 Assessment of the simulation

The experimental situation sketched in Fig. 4 is fully characterised by the Reynold number (Re), defined as

$$\mathrm{Re} = UL\rho/\eta, \tag{8}$$

with a characteristic length L, average velocity U, density ρ and viscosity η. In our case, the relevent length is the channel height, which is much smaller than the overall length of the chamber. Thus, we can conveniently compare velocity fields $u(x, y, z)$ by contour plots of a Reynolds number that depends on position,

$$\widetilde{\mathrm{Re}}(x, y, z) = u(x, y, z)L\rho/\eta. \tag{9}$$

$u(x, y, z)$ is the (non-directional) absolute value of the velocity vector field at point (x, y, z). Experimentally, $\widetilde{\mathrm{Re}}$ can be estimated to range between 0.5 and 10.0, with typical average flow velocities of 1−3 cm/s. Thus, although one is dealing with the regime of laminar flow, it is not permissible to treat the system in some asymptotic limit such as Stokes flow, assuming $\mathrm{Re} \ll 1$. This also holds for the hydrodynamic drag force F_d exerted on a microsphere. F_d can be expressed by its relative velocity v with respect to the local flow field, its cross sectional area $A = \pi R_0^2$ and a drag coefficient C_d that is a function of Re only,

$$F_d = KAC_d, \quad C_d = f(\mathrm{Re}), \tag{10}$$

where K is the kinetic energy $K = \frac{1}{2}\rho v^2$ per unit volume. Equation 10 is a general expression summarizing several analytical expressions that can be found in literature (Johnson 1998; Bird et al. 2002). With respect to the dynamics of the microspheres the influence of the residual fluctuations received from the *FP*s of the surrounding liquid must also be accounted for. If all other forces on the beads compared to the thermal fluctuations are small, their Brownian motion becomes dominant. For a bead initially at rest at $x = 0$, the uncertainty of position after a time interval Δt is characterized by the average mean square deviation $\langle \Delta x^2 \rangle$ and is proportional to $D_{\mathrm{dif}}\Delta t$, where $D_{\mathrm{dif}} = k_B T/6\pi\eta R_0$ is the Einstein expression for the diffusion coefficient of a spherical particle of radius R_0. This becomes relevant if the bead diameter becomes smaller than roughly 1 μm; in order to represent the experimental situation with diameters larger than, e.g.,

100 μm, the diffusive broadening in position must be negligible after the sphere has traveled a typical distance l (say, the distance from inlet to outlet of the aggregation chamber). We can thus characterize the relative importance of thermal motion by a Peclet number

$$Pe = \frac{Ul}{D_{\text{dif}}}, \tag{11}$$

This way we can estimate a lower bound of $Pe \sim 2{,}300$ [with $R_0 = 2.5\ r_c$, $l = 204\ r_c$ and $U = 0.2$], which is significantly larger than 1.

Finally, the Mach number Ma is of some importance. $\text{Ma} = v/c$ relates the velocity v of a moving object in the liquid to the velocity of sound c; for $\text{Ma}^2 \sim 1$ significant deviations from the equilibrium fluid density are to be expected (Landau and Lifshitz 2004). Conversely, v could be taken as the streaming velocity of the fluid right before obstacles or at corners. For laminar flow Ma is usually negligibly small. In a typical *DPD* simulation rather large values of Ma can result (Kim and Phillips 2004) on account of the soft interparticle interactions. For our case, we encounter a maximum $\text{Ma}^2 \approx 0.09$, consistent with the observation that during all simulations the liquid density is constant within numerical errors.

The above assessment aims at a continuum description characterized by dimensionless numbers, and thus there is no need to match the properties of the *DPD* liquid to those of the real fluid in a one-to-one fashion. In Groot and Rabone (2001), for example, such a correspondence has been established by comparing statistical mechanical properties of the real and the model liquid. In our case, properties such as diffusivities of small dispersed objects or even single *FP* only limit the choice of scale. Defining a length scale of $r_c = 30$ μm (the bead assay, Sect. 5) or $r_c = 25$ μm (flow constriction, Sect. 3) is a compromise between numerical efficiency and keeping the Peclet number (Eq. 11) as large as possible, as D_{dif} is set by the bead radius R_0 (in *DPD* units); but r_c could have been any smaller length, but thereby increasing the overall number of *FP* representing the system. Similarly, a relatively low value of the Schmidt number *Sc* ($1 < Sc < 10$ in our case) can be tolerated—*Sc* is the ratio of kinematic viscosity and the diffusivity of a single *FP*; small values of *Sc* imply that viscosity mainly originates from momentum diffusion by particle diffusion, similar to a gas. A large value of *Sc* implies a small time step (Lowe 1999).

In what follows, we present an explicit validation representative for a class of systems similar to the aggregation chamber. In order to test flow profiles and boundary conditions, we choose a somewhat simplified reference system depicted in Fig. 5. It consists of a double constriction connected by a thin rectangular flow channel (simulation parameters are given in Table 1). At this point it is important to discuss the ways of setting appropriate pressure or velocity boundary conditions.

3.3 Flow field in confined geometries, boundary conditions

For the DPD scheme, the assignment of boundary conditions at inlets/outlets is much more difficult than in CFD,

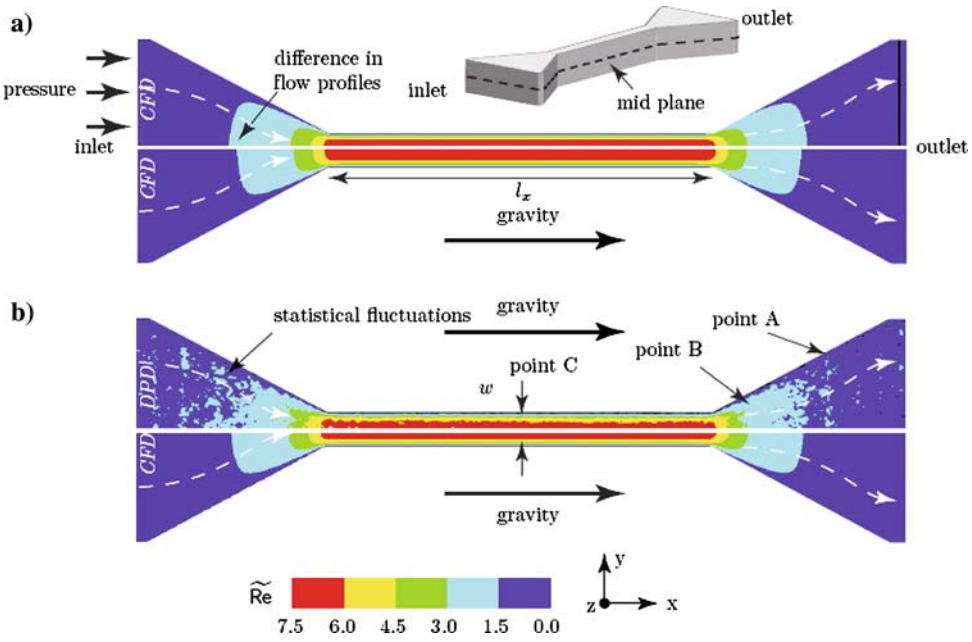

Fig. 5 Flow profiles of water in a constriction–expansion of length $l_x = 5{,}000$ μm, width $w_x = 400$ μm and height 190 μm with a transformation factor of 1 $r_c = 25$ μm from it CAD design to it FP-geometry. **a** Comparison of two it CFD simulations, with water driven by pressure (*upper*) or gravity (*lower*). The small difference in the flow profiles arises from $\nabla p = -\bar{\rho}\mathbf{g}$. **b** Comparison between it DPD and it CFD simulations. The velocities of it FPs are averaged over 20,000 time steps after 10,000 time steps of equilibration (color online)

Table 1 Flow field *DPD* and *CFD*

Parameter	
FP simulation	
Simulation size	400 r_c × 115 r_c × 9 r_c
Density of fluid ρ	5.0
Viscosity of fluid η	1.78
CPUs	8
No. of *FP*s	901,953
No. of time steps	30,000
Time step	0.02
A_{fw}	50
A_{ff}	25
σ	5
CFD simulation	
Density of fluid ρ	1 g/cm^3
Viscosity of fluid η	0.001 Pa s
Body force (gravity)	6.2 m/s^2
Length of scale	1 μm

whereas a given flow rate can be established by employing "pistons" (realized by time-varying external forces) that move with constant velocities along fluidic terminals, setting a given pressure difference is more difficult. Strictly speaking, dealing with a statistical thermodynamical system one should set pressure boundary conditions by specifying appropriate chemical potentials at the fluidic ports of the structure (Nicholson et al. 1995). However, these exact methods are rather awkward to implement, as fluid particles have to be continuously created or removed from the simulation, and are prone to instabilities.

For practical purposes, rather few alternatives are offered. We briefly sketch two alternatives that we have implemented and tried out. Sun and Ebner (1992) establish a pressure difference by having the particles in one terminal reservoir expand freely into the system, while keeping the reservoir density constant by the action of a piston. As soon as particles enter an outlet they are simply removed. For the *DPD* system we found that these pressure boundary conditions frequently lead to undesired pressure oscillations throughout the whole system. The "reflecting boundary method" of Yip (Li et al. 1998) appears more stable instead. With this scheme, suitable reflection–transmission probabilities are prescribed for particles crossing specific virtual planes located and inlet and outlet. The resulting bias on the direction of flight establishes an effective pressure difference, a fluid initially at rest is set in motion, and for a straight channel a well-defined Poisseuille flow profile develops. An advantage of this method is a compatibility with periodic boundary conditions. Between the terminals containing the reflection planes the channel geometry may also vary. But the pressure generated is not a unique function of the reflection probabilities, nor of the channel geometry. Thus, although technically simple this method appears rather cumbersome in practice. For the present purposes with rather linear geometries, which might actually apply to a number of similar cases, we have found that application of simple body forces (artificial gravitation) gives quite satisfactory results. In straight channels of constant cross section, a constant body force $\mathbf{F}_i^{\text{ext}}$ acting on each particle will generate a constant pressure gradient $\nabla p = -\bar{\rho}\mathbf{g}$ and thus a parabolic Poisseuille flow profile. In channels of varying cross section one must expect deviations to occur compared to applying exact pressure boundary conditions, but Fig. 5 suggests that at least for the present case these deviations are quite tolerable. In Fig. 5a, we contrast velocity profiles of two *CFD* simulations, one with pressure boundary conditions and the other with an equivalent body force (same total pressure drop across the channel). In the color-coded profiles of $\widetilde{\text{Re}}$, acquired along the horizontal mid-plane, only small differences are noticeable. In Fig. 5b, a *DPD* simulation with 20,000 time steps of averaging is compared to the *CFD* results with respect to the body force. The coarse color scale overemphasizes the residual fluctuations in the velocity field, the agreement is actually quite excellent. In Fig. 6, we compare $\widetilde{\text{Re}}$ acquired across the middle of the connecting channel (point C) in comparison to the analytical solution for the $x-$component $u_x(y, z)$ for a rectangular channel with $-a \le y \le a$ and $-b \le z \le b$ (Johnson 1998),

$$u_x(y,z) = -\frac{16a^2}{\eta\pi^3}\left(-\frac{dp}{dx}\right) \times \sum_{i=1,3,\ldots} (-1)^{\frac{i-1}{2}}\left[1 - \frac{\cosh(i\pi y/a)}{\cosh(i\pi b/2a)}\right]\frac{\cos(i\pi z/a)}{i^3}, \tag{12}$$

with $2b = 7.5\ r_c$, $2a = 16\ r_c$ and $r_c = 25\mu$m. This is feasible as in the long connecting channel the pressure gradient dp/dx is nearly constant. The analytical solution is reproduced within error bars. Note that the extrapolation of the velocity profile to the channel boundaries indicates that indeed no-slip boundary conditions apply, although the corresponding snapshot in the upper graphics clearly shows significant particle layering, typical of flat solid boundaries as mentioned above.

3.4 Hydrodynamic drag

Apart from flow fields, drag forces exerted on dispersed beads will be checked. On the one hand this is necessary as, for efficiency reasons, in the simulation, the beads are created "on the fly" out of a rather small number of fluid particles, contained in a spherical volume fluid (47 fluid particles, see Fig. 8a), by freezing their relative motion; the

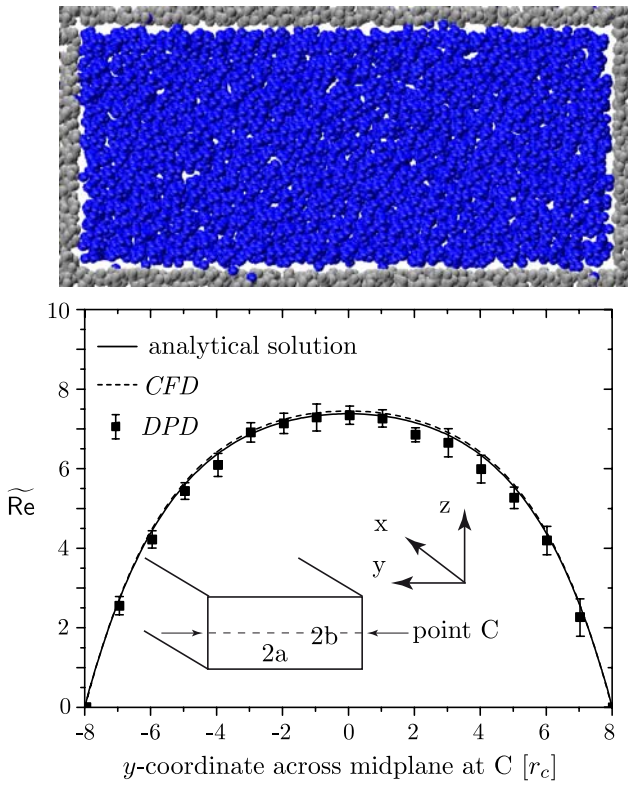

Fig. 6 Flow profiles of *CFD*- and *DPD*-simulation with a corresponding analytical solution in a long narrow three dimensional channel as depicted in Fig. 5. The *upper panel* shows a slice 10 r_c thick, centered at C, of a snapshot of the particle configuration. *Gray*: frozen boundary particles, *blue*: fluid particles. The density of particles in the boundary is the same as in the liquid (color online)

same configuration will be used in the aggregation simulations. The resulting shape of the microsphere is rather rough and it is not clear from the beginning if on short time average, the *FP* bead appears as a structureless spherical object.

On the other hand, it is also particularly interesting as within the regime of laminar flow, one frequently associates hydrodynamic drag with a simple analytical expression such as the well-known *Stokes law*

$$F_d = 6\pi\eta R_0 v_\infty, \tag{13}$$

predicting that the drag force F_d depends linearly on the bead velocity v_∞, R_0 is again the radius of a microsphere. Expressing the drag force in terms of the general form (Eq. 10), the drag coefficient C_d reads

$$C_d = \frac{24}{\mathrm{Re}} \quad \text{for} \quad \mathrm{Re} \ll 0.1. \tag{14}$$

But the simulations as well as experiments in this work are carried out for $0.5 < \mathrm{Re} < 10$. It is interesting to note that even involved analytical, higher order corrections (Proudman and Pearson 1957; Chester et al. 1969)

$$C_d = \frac{24}{\mathrm{Re}} \cdot \left[1 + \frac{3}{16}\mathrm{Re} + \frac{9}{160}\mathrm{Re}^2 \times \left(\ln\left(\frac{1}{2}\right) + \gamma + \frac{5}{3}\ln(2) - \frac{323}{360} \right) + \frac{27}{640}\mathrm{Re}^3 \ln\left(\frac{1}{2}\mathrm{Re}\right) + O(\mathrm{Re}^3) \right] \quad \text{for} \quad \mathrm{Re} < 1.0, \tag{15}$$

are approximately valid only up to $\mathrm{Re} \sim 1$ ($\gamma = 0.5772$ is Euler's constant). Figure 7 shows that already for $\mathrm{Re} > 1$ only an empirical expression for C_d (Abraham 1970; Vandyke 1971)

$$C_d = \left(\sqrt{\frac{24}{\mathrm{Re}}} + 0.5407 \right)^2 \quad \text{for} \quad \mathrm{Re} < 6000.0, \tag{16}$$

compares well to the numerically determined values. In the simulations C_d is determined by driving one single bead through a sufficiently large fluidic volume (length, height and width of 40.8 r_c × 15.3 r_c × 15.3 r_c), filled with fluid of density $\rho = 3.5$. Periodic boundary conditions are applied in all three directions. The remaining simulation parameters are summarized in Table 2. The bead is placed in the box center and driven at a constant force $\mathbf{F}_D$ along the long axis. In an actual experiment, a bead would be driven through a fluid at rest. To realize this condition with a finite simulation box, a thin slice (0.5 r_c thick) of fluid particles was frozen (velocities set to zero) at every time step at constant distance away from the bead (half of the box length). As the slice is moving, it is constantly yielding fluid that quickly equilibrates at zero average velocity. This way, a well-defined temperature can be kept and a stationary velocity develops which is then averaged over 50,000 time steps and used to determine Re. In Fig. 7, C_d determined this way is displayed and compared with the

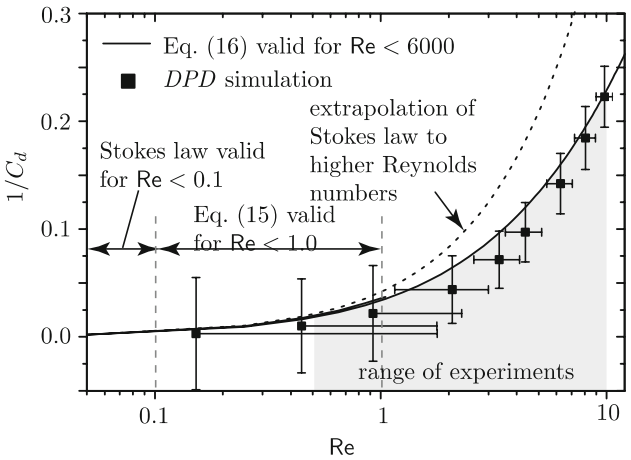

Fig. 7 Inverse drag coefficient for a *DPD* bead of radius 2.5 r_c and fluid of density $\rho = 3.5$

Table 2 Hydrodynamic drag on a bead

Parameter	Value
Time step dt	0.02
A_{ff}	25.0
A_{fb}	25.0
Density of fluid ρ	3.5
Effective radius of bead R_b	2.5
No. of *FP*s per bead	141

drag coefficients resulting from Eqs. 14–16. Within error bars, the drag coefficient from the simulation results agrees with the interpolating empirical expression from Eq. 16, implying effective stick boundary conditions on the bead surface. This encouraging finding is in accord with the analysis of the flow fields—hydrodynamic details of laminar flow are well represented by the *DPD* approach.

4 Representation of beads with quaternion dynamics

Dispersed objects advected with fluid flow can be most conveniently modeled as a compound rigid fluid particle configuration, i.e., a set of particles with fixed relative positions $\mathbf{r}_{\text{rel}}$ but with a mobile center of mass (*COM*) and axes of inertia. The obvious alternative of connecting the constituting particles by stiff springs will, in case of rigid bodies, not only require an unnecessarily small time step but also does not guarantee that the initially chosen object shape can be kept throughout the simulation (due to mechanical instabilities). Generation of rigid objects and introducing them into the fluid is most conveniently carried out "on the fly", as illustrated in Fig. 8a). (i) First, a set of *FP*s within the liquid is chosen to define the shape of the object. (ii) The relative motion of those particles is frozen and the further dynamics is solely governed by (iii) *COM* motion which is independent of it the rotational dynamics of the body axes, with appropriate moments of inertia. Forces and torques on an object are computed simply by summing up all contributions of neighboring solvent particles. This procedure is easily used to insert beads into the simulation at a specified time and location. This is how the bead injector shown in Fig. 4 is realized.

Whereas the translation is handled in the same way as for single particle motion, computing the rotation by straightforward schemes such as Euler-angles (Evans and Murad 1977; Goldstein 1980) or the body vector method (Evans 1977) can become quite cumbersome if, as in the present case, a few hundred or even thousands of objects are involved. We shall therefore outline briefly the method of so called quaternion dynamics (Allen and Tildesley

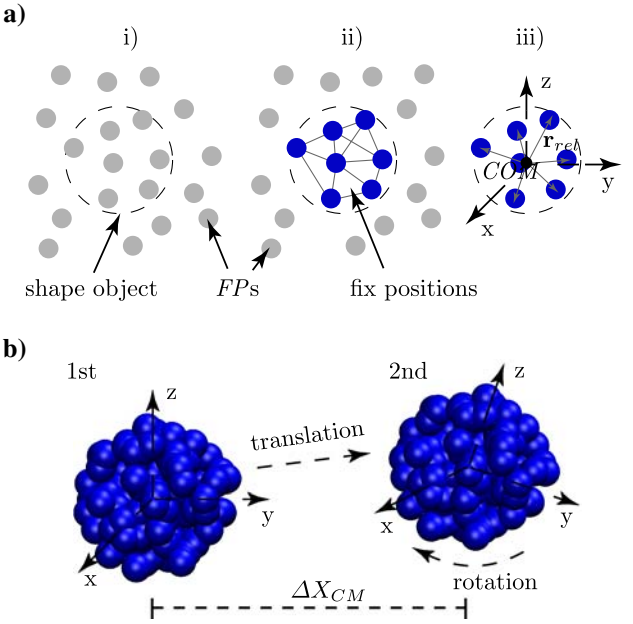

Fig. 8 **a** Generation of an extended object in three steps. (*i*) Define the shape of an object. (*ii*) Freeze *FP*s together. (*iii*) Calculate the center of mass as well as the moments of inertia. **b** The dynamics of three dimensional extended objects is described by quaternion dynamics with independent translation and rotation (color online)

1987; Goldstein 1980) that we have used throughout and that has various numerical advantages. Yet it does not appear to be frequently used in practical engineering problems. The basic idea of quaternion dynamics is that all quantities such as orientation or angular velocity are first transformed into a body-centered coordinate frame. In this frame, the orientation of the object is determined by *four* parameters, $\mathbf{q} \equiv (\chi, \eta, \xi, \zeta)$ (the "quaternion"), the components of which are related to the three Euler-angles θ, ψ, ϕ by the equations

$$\begin{aligned} \chi &= \cos(\theta/2)\cos(\psi+\phi)/2, \\ \eta &= \sin(\theta/2)\cos(\psi-\phi)/2, \\ \xi &= \sin(\theta/2)\sin(\psi-\phi)/2, \\ \zeta &= \cos(\theta/2)\sin(\psi+\phi)/2. \end{aligned} \tag{17}$$

In expressing rotational dynamics by $\mathbf{q}$, the singularities and also excessive numerical evaluation of trigonometric functions are avoided (Evans and Murad 1977; Goldstein 1980). Corresponding to Eq. 17 the matrix of rotation for Euler-angles $\mathbf{R}(\theta, \phi, \psi)$ is related to a rotational matrix $\mathbf{A}(\mathbf{q})$ in the quaternion description by

$$\mathbf{A}(\mathbf{q}) = \begin{pmatrix} -\xi^2+\eta^2-\zeta^2+\chi^2 & 2(\zeta\chi-\xi\eta) & 2(\eta\zeta+\xi\chi) \\ -2(\xi\eta+\zeta\chi) & \xi^2-\eta^2-\zeta^2+\chi^2 & 2(\eta\chi-\xi\zeta) \\ 2(\eta\zeta-\xi\chi) & -2(\xi\zeta+\eta\chi) & -\xi^2-\eta^2+\zeta^2+\chi^2 \end{pmatrix} \tag{18}$$

with the constraint $\mathbf{q}^2 = \chi^2 + \eta^2 + \xi^2 + \zeta^2 = 1$.

With $\mathbf{A}(\mathbf{q})$ any vector in the laboratory frame such as the angular velocity $\boldsymbol{\omega}_{lf}$ is transformed into the quaternion description $\boldsymbol{\Omega}_q$,

$$\boldsymbol{\Omega}_q = \mathbf{A}(\mathbf{q})\boldsymbol{\omega}_{lf}. \tag{19}$$

The time derivative $\dot{\mathbf{q}} \equiv (\dot{\xi}, \dot{\eta}, \dot{\zeta}, \dot{\chi})$ is related to the principal angular velocities $\boldsymbol{\Omega}$ by (Omelyan 1998)

$$\dot{\mathbf{q}} \equiv \frac{1}{2}\mathbf{Q}(\mathbf{q})\boldsymbol{\Omega} = \frac{1}{2}\begin{pmatrix} -\zeta & -\chi & \eta & \xi \\ \chi & -\zeta & -\xi & \eta \\ \xi & \eta & \chi & \zeta \\ -\eta & \xi & -\zeta & \chi \end{pmatrix}\begin{pmatrix} \Omega_x \\ \Omega_y \\ \Omega_z \\ 0 \end{pmatrix} \tag{20}$$

With the transposed $(\mathbf{Q})^{\mathrm{T}}$ of the orthogonal matrix $\mathbf{Q}$ the principal angular velocity can be calculated to $\boldsymbol{\Omega} = 2(\mathbf{Q})^{\mathrm{T}}(\mathbf{q})\dot{\mathbf{q}}$, and the second time derivative of Eq. 20 gives Newton's equations for $\mathbf{q}$:

$$\ddot{\mathbf{q}} = \frac{1}{2}(\mathbf{Q}(\dot{\mathbf{q}})\boldsymbol{\Omega} + \mathbf{Q}(\mathbf{q})\dot{\boldsymbol{\Omega}}). \tag{21}$$

According to the Euler equation, the angular acceleration $\dot{\Omega}$ in the body frame is (Omelyan 1998)

$$\dot{\Omega}_x = \frac{T_x + (I_y - I_z)\Omega_y\Omega_z}{I_x} \tag{22}$$

with moments of inertia I and torque T of the object. To be consistent to the *Velocity-Verlet* algorithm of the point particles we also used a *Velocity-Verlet* form of the integration scheme for quaternions as described by Martys and Mountain (1999) or the earlier approach of Omelyan (1998a, b) which is described in detail in Appendix B.2. The quaternion approach can be used for any object shape.

5 Beadaggregation: simulation versus experiment

After the extensive validation procedure of the previous section, we can finally consider the case of successively aggregating microspheres and compare experimental measurements to corresponding simulations. Figure 9 captures in four snapshots the progress of aggregation in the simulation as opposed to the experiment. Table 3 summarizes the parameters for the corresponding simulation setup. Note that to optimize numerical efficiency, a slightly larger time step and a lower density have been used as compared to the other simulations. This also implies a lower viscosity (see Groot and Warren 1997). A length of 1 r_c in the simulation here corresponds to a real length of 30 μm. The process of bead injection proceeds as described in Sect. 3, with beads injected within the neck of the geometry, at a distance of $d_{\mathrm{bi}} = 12\ r_c$ away from the inlet of the aggregation chamber. In the experiments, a bead-suspension is introduced at the inlets with an averaged bead flow rate of $I_{\mathrm{bi}}^{\mathrm{exp}} = 28^{\mathrm{beads}}/\mathrm{s}$ and the filling process is finished after approximately 12 *s* with 335 aggregated beads. The maximum Reynolds number at the inlets was $\mathrm{Re}_{\mathrm{max}} = 5.4$ falling down to $\mathrm{Re}_{\mathrm{min}} = 0.7$ in the middle of the aggregation chamber. Similar to the double constriction considered earlier, we chose a gravitational body force (not acting on the microspheres) to drive the fluid flow. A simulation with a maximum time step of $dt = 0.03$ would require in our case the calculation of roughly 1.2 million iterations. However, due to the computer access available we had to guarantee that the whole filling process can be calculated within 1 week on 32 processors, distributed over several time slices (a brief sketch of the coding and computer platforms employed is given in Appendix A). This made it necessary to "speed up" the aggregation in the simulations accordingly, and thus the Reynolds numbers have been chosen $\approx 60\%$ higher ($\sim \mathrm{Re}_{\mathrm{max}} = 8.6$), while at the same time increasing the injection rate to approximately $I_{\mathrm{bi}}^{\mathrm{sim}} = 47^{\mathrm{beads}}/\mathrm{s}$. (the simulation parameters for the bead aggregation simulation are summarized in Table 3). In the presented visualization we rescaled the time of the simulation by the ratio of Reynolds numbers to achieve an equivalent time to the experiments $t_{\mathrm{eq}}^{\mathrm{sim}}$

$$t^{\mathrm{exp}} \hat{=} t_{\mathrm{eq}}^{\mathrm{sim}} = t^{\mathrm{sim}} \cdot \frac{\mathrm{Re}^{\mathrm{exp}}}{\mathrm{Re}^{\mathrm{sim}}}. \tag{23}$$

This allows us to compare the time-dependent fronts of the bead stacks. The excellent overall agreement between simulation and experiment can be directly inferred from Fig. 9a–d. The bead flow expands at the enlarging inlet and aggregation starts at the outlet corner of the microfluidic structure. In detail, the aggregation proceeds as follows: the fluidic resistance along the chamber is smallest along its center, and the first microspheres accumulate directly at the corner of the step. This in turn increases the fluidic resistance in the center of the channel. In the evolving agglomerate of microspheres, newly arriving beads are thus naturally directed towards possible voids and gaps, and this sort of self-organization gives rise to a uniformly growing front seen in both, simulation and experiment.

There are, however, significant differences, such as the disorder of stacked beads seen in the experiments is not present in the simulation. In the experiment, the spheres tend to stick to each other and towards the PMMA-boundaries of the chamber. In addition, there must be significant friction forces as the initial configuration of microspheres beyond the rightmost dashed white line in Fig. 9a–d virtually does not change through the four snapshots. In contrast, the spheres created in the simulation appear "slippery", and give rise to an almost perfect hexagonal packing. This is surprising at first sight. By construction, their surfaces should bear a certain roughness as seen in Fig. 10 and one should expect a similar irregular stacking. The reason for this unexpected behavior is the following: the mutual interaction between beads has been

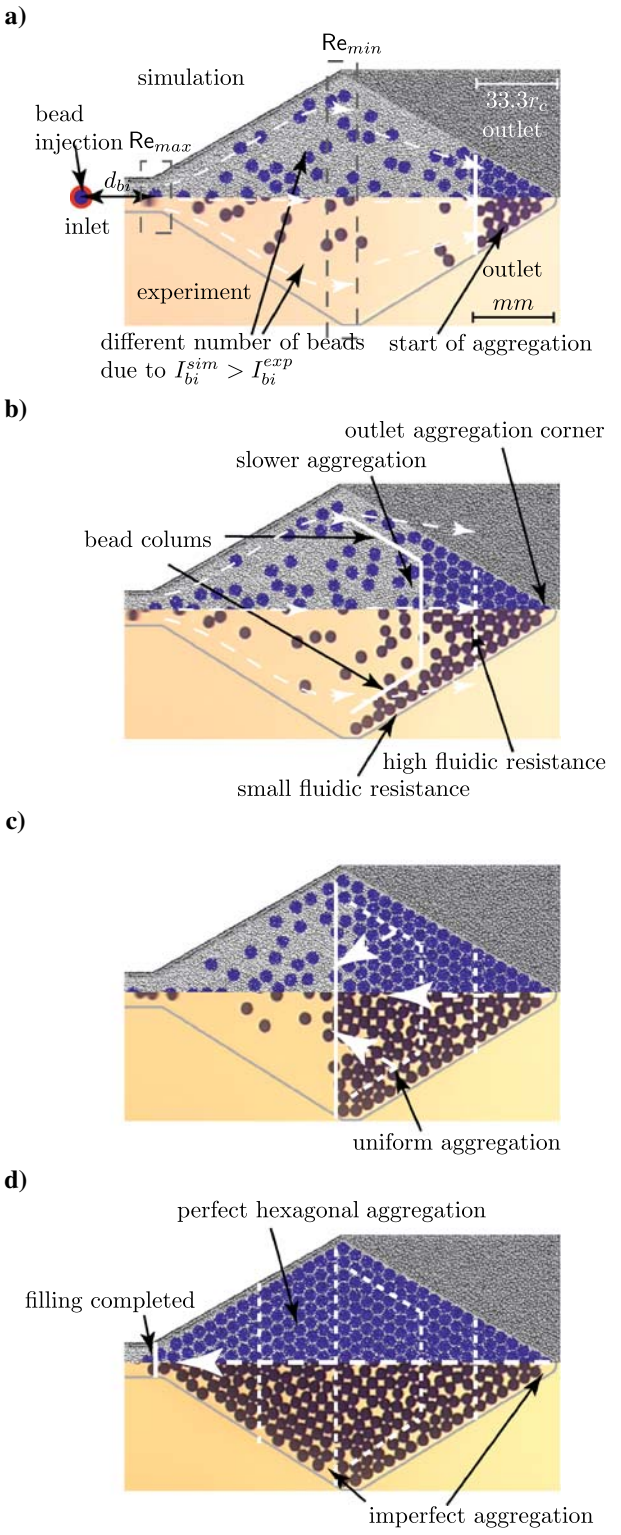

Fig. 9 Simulation and experiments of aggregating beads at comparable Reynolds number range. Simulation settings are given in Table 3. **a** $t^{exp} = 2.0$ s, **b** $t^{exp} = 3.0$ s, **c** $t^{exp} = 6.0$ s, **d** $t^{exp} = 12.0$ s (color online)

kept purely repulsive as, e.g., between the liquid and the solid walls. They do not feel their surface corrugation sufficiently, and interact effectively as nearly smooth

Table 3 Microfluidic aggregation chamber

Parameter	Value
Size simulation	204 r_c × 81.6 r_c × 7.14 r_c
Time step dt	0.03
Density of fluid ρ	3.5
Viscosity of fluid η	1.2
A_{ff}	25.0
A_{fb}	25.0
A_{fw}	50.0
A_{bw}	200.0
A_{bb}	200.0
σ	5.0
Radius of bead R_b	2.5
Gravity force	1.0

spherical objects (cf Fig. 10a). They may slip past each other, with the dissipative force as the only source of friction between them. But depending on relative velocity, this force allows for creeping motion that cannot be halted completely. In this context, the residual stochastic rotational motion, which is clearly visible within the stack also helps removing jammed bead arrangements. In the experiment it is indeed possible to achieve a perfect hexagonal aggregation by carefully choosing additives such as salts to change the repulsion of the electrical double layers around the spheres, or tensides to alter the wettability of the microspheres as shown in Grumann et al. (2004). Conversely, the microspheres in the simulation can be made "stickier" by simply reducing their mutual repulsion. This will lead to a closer approach and in turn also increase the effect of surface corrugation, see Fig. 10b). Now the jammed stacking is stable. However, the reduction of mutual repulsion necessary to achieve stick has made the beads too hydrophobic with respect to the solvent, microspheres tend to lump to form larger aggregates, and the packing is apparently too dense as compared to the arrangement in Fig. 9a–d, as the soft interactions between microspheres allow for their overlapping.

The point is that modeling the hard sphere character of the microbeads and their interactions actually comprises a variety of mechanisms and forces spanning several length scales, such as electrostatic, elastic and other short range surface forces. At the present level of modeling these phenomena cannot be represented. This situation is typical of particle-based simulation approaches such as the simple *DPD* scheme used in this work, employing only a single length scale. In order to refine the aggregation behavior in the simulation, one can nevertheless introduce additional effective forces employing, e.g., concepts developed for describing the dynamics of powders and grains with additional normal and tangential forces between extended

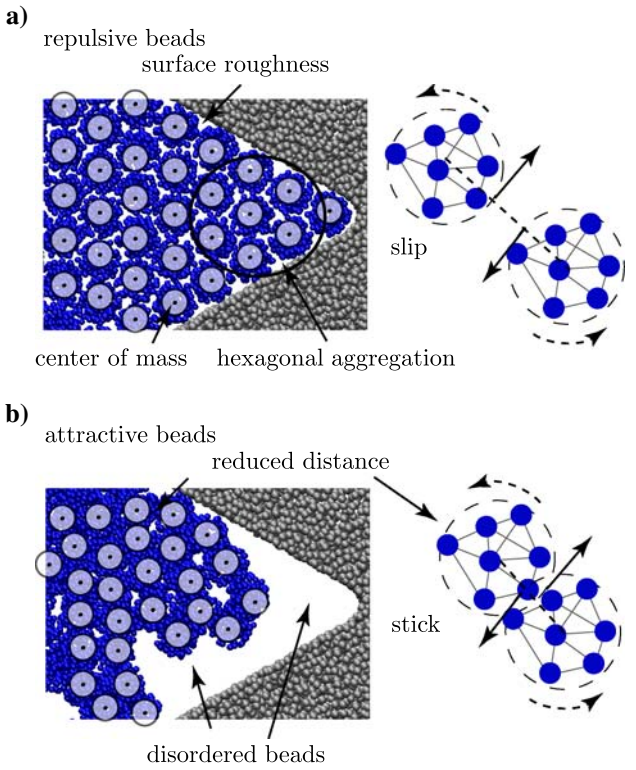

Fig. 10 **a** All *FP*s of the beads are kept purely repulsive, which generates slip and lead to a regular hexagonal ordering in a suitable structure. **b** Adhesive beads interact at the outer limits via attractive forces while *FP*s inside the object are repulsive to prevent beads merging together (color online)

objects (Cundall and Strack 1979; Luding 2005). An implementation of a new type of force will in general introduce another length scale to the system, possibly with correspondingly reduced integration time steps. On the other hand, these forces may act only between a relatively small number of objects, compared to the total number of particles constituting the simulation such that the overall numerical efficiency is not affected.

6 Conclusion

To our knowledge this has been the first time a *DPD* simulation scheme has been put to the test in a realistic design used for constructing an actual microfluidic device. We find that using the method as a separate tool (not numerically linked to a *CFD*-scheme) is most efficient, as hydrodynamics, solid boundaries and interacting dispersed objects are all treated under one wing. The resulting versatility is clearly a strength of the method. For representing the problem of the bead assay, we have used a rather simple version of *DPD* which is essentially the one described in Groot and Warren (1997). The purpose was to show the nature of the simulation method, its virtues and also its limitations. In the process of validation it has become apparent that hydrodynamics in channels and with dispersed interacting objects is represented faithfully, even without exercising excessive care in setting up the simulation—flow fields and drag forces are represented up to residual statistical errors, at the channel boundaries the no-slip boundary condition is obeyed without additional effort. Only the accurate prescription of pressure boundary conditions (possibly at various terminals) still remains a technical challenge.

One may summarize that for laminar flows, one has a reliable, explicit model for the solvent that may host a variety of structured objects—these may represent polymers, vesicles or colloids or beads, and the full hydrodynamic interactions between them are included. Carrying out a conscious validation process as outlined in this work permits to identify precisely the limitations of the particular scheme used. In our case this has been the lack of representing multiple length scales or equivalently, a lack of specialized effective interactions. These, however, may be added successively in order to emulate the required behavior. In fact, thinking in terms of successive approximations by refining force laws might play a major role for designing future commercial products involving *DPD*. The necessity of using varying levels of description in the particle-based method must not be viewed as a deficiency, but as a strength of the method. One is able to turn distinct effects on or off, depending on what is to be learned about the system in question. In this respect, the scheme is a powerful explorative tool.

Acknowledgments The support of the Landesstiftung Baden-Württemberg (HPC-Project) is gratefully acknowledged.

Appendix A: Coding and computer platforms

For simulating the types problems presented in this work we developed a parallelized simulation code based domains, and each domain is associated with a computational node (processor or processor core). Since the *DPD* interparticle interaction is of relatively short range, a given domain need only know about the particles within a thin (of the order of 1 r_c) adjacent border of neighboring domains. That is, most of the time a given process unit can work quite autonomously. This behavior is most easily implemented with only elementary routines of the *Message Passing Interface* (*MPI*). *MPI* is available on nearly every hardware platform ranging from single laptops up to huge cluster systems with hundreds of processors (Dongarra et al. 1994). In coding our applications, we essentially follow Griebel et al. (2004). We stick to a strict domain decomposition, except for treating rigid objects that may be

much larger than the cutoff radius. As each microsphere in the simulation is of the same particle configuration, it is convenient that each process unit has the information of *all* objects, facilitating the computation of the forces acting on a specific microsphere.

We note that useful information about the problem can already be extracted from a typical simulation run taking 10–12 h on a cluster with 32 processors. This involves, e.g., the aggregation of a swarm of beads traversing the chamber simultaneously. The corresponding computational resources should be available at almost every research facility nowadays. The presented sequential filling of beads takes about 6 days on 32 processors with up to 650,000 time steps and 500,000 *FP*s on a Linux cluster (NEC Xeon EM64T) of the high performance computing center in Stuttgart (http://www.hlrs.de). The issue of size, i.e., the number of *DPD* particles needed to represent a certain situation, which played a role in this work, may soon lose importance. Low-cost workstations with 4 processors and 16 cores will become standard soon, and the simulations carried out in this work will not even require a PC-cluster, and one could also dispose of some of the tricks (reduction to periodic boundary conditions, bead injector) necessary in the present work to enhance numerical efficiency.

Appendix B: Simulation algorithm

B1: Velocity-Verlet algorithm for DPD

In the conventional *Velocity-Verlet* algorithm for conservative forces, there are three stages (Allen and Tildesley 1987; Swope et al. 1982). First, the positions at time $(t+\Delta t)$ and the mid-step velocity at time $(t+\frac{1}{2}\Delta t)$ are calculated

$$\mathbf{r}(t+\Delta t)=\mathbf{r}(t)+\Delta t\mathbf{v}(t)+\frac{1}{2m}\Delta t^2\mathbf{f}(t) \tag{24}$$

and then the forces with the positions at time $(t+\Delta t)$,

$$\mathbf{f}(t+\Delta t)=\mathbf{f}(\mathbf{r}(t+\Delta t)), \tag{25}$$

and the new velocity is obtained as

$$\mathbf{v}(t+\Delta t)=\mathbf{v}(t)+\frac{1}{2m}\Delta t[\mathbf{f}(t)+\mathbf{f}(t+\Delta t)]. \tag{26}$$

In the *DPD* scheme the force is velocity-dependent, and a prediction is needed for the velocity at $t+\Delta t$. If, according to Groot and Warren (1997) the algorithm is modified with

$$\begin{aligned}\tilde{\mathbf{v}}(t+\Delta t)&=\mathbf{v}(t)+\lambda\Delta t\mathbf{f}(t)\\ \mathbf{f}(t+\Delta t)&=\mathbf{f}(\mathbf{r}(t+\Delta t),\tilde{\mathbf{v}}(t+\Delta t))\end{aligned} \tag{27}$$

time steps up to $\Delta t=0.05$ with sufficient temperature control. The influence of the integration scheme and the behavior of a particular system with respect to the time step has been discussed in Peters (2004) and references therein.

B2: Velocity-Verlet algorithm for quaternions

It is assumed that there exists one coordinate system *XYZ* fixed in an inertial frame and an individual body-centered coordinate systems xyz_k fixed in their center of mass (*CM*). At first, the position $\mathbf{r}^k_{CM}$ of the bead k, its mid-point velocity $\mathbf{v}^k_{CM}$ and its mid-point angular velocity $\mathbf{\Omega}^k_{CM}$ is calculated to

$$\mathbf{r}^k_{CM}(t+\Delta t)=\mathbf{r}^k_{CM}(t)+\mathbf{v}^k_{CM}(t)\Delta t+\frac{\Delta t^2}{2}\frac{\mathbf{f}^k_{CM}(t)}{m^k_{CM}} \tag{28}$$

$$\mathbf{v}^k_{CM}(t+\frac{1}{2}\Delta t)=\mathbf{v}^k_{CM}(t)+\frac{\Delta t}{2}\frac{\mathbf{f}^k_{CM}(t)}{m^k_{CM}} \tag{29}$$

$$\mathbf{\Omega}^k_{CM}(t+\frac{1}{2}\Delta t)=\mathbf{\Omega}^k_{CM}(t)+\frac{1}{2}\dot{\mathbf{\Omega}}^k_{CM}(t)\Delta t \tag{30}$$

Here $m^k_{CM}=\sum m_i$ and $f^k_{CM}=f_i$ are the total mass of bead k and the total force acting on it. Position and velocity of the bead are calculated with respect to the laboratory frame *XYZ* whereas the angular velocity is calculated with respect to its body centered frame xyz_k.

In the second step the total force f^k_{CM} acting on the bead is calculated by summing-up all forces f_i of the *FP*s inside the bead that are previously calculated in the *Velocity-Verlet* algorithm for *FP*s (cf Sect. 2).

$$\mathbf{f}^k_{CM}(t+\Delta t)=\sum_{i=1}^{nat^k}\mathbf{f}_i(t+\Delta t) \tag{31}$$

In a last step the velocity as well as the angular velocity of the beads are updated to time $(t+\Delta t)$.

$$\mathbf{v}^k_{CM}(t+\Delta t)=\mathbf{v}^k_{CM}(t+\frac{1}{2}\Delta t)+\frac{\Delta t}{2}\frac{\mathbf{f}^k_{CM}(t+\Delta t)}{m^k_{CM}} \tag{32}$$

$$\begin{aligned}\Omega^{(n)}_x(t+\Delta t)=\Omega_x(t)+\frac{\Delta t}{2I_x}\Big\{&T_x(t)+T_x(t+\Delta t)\\&+(I_y-I_z)\Big[\Omega_y(t)\Omega_z(t)\\&+\Omega^{(n-1)}_y(t+\Delta t)\Omega^{(n-1)}_z(t+\Delta t)\Big]\Big\}\end{aligned} \tag{33}$$

Here the angular velocity is updated via an iterative procedure in n using Omelyan's scheme (cyclic with y and z) where only 3–5 iterations are sufficient to gain good results for the current time step (Omelyan 1998).

After the dynamics of the whole object k is calculated the new positions and velocities of the *FP*s inside the bead have to be updated with respect to its *COM*. Because the *FP*s are updated in the inertial frame their relative positions Δ^k_i and angular velocities $\mathbf{\Omega}^k$ in the body-centered frame first have

to be transformed back with the transposed of the rotational matrix $\mathsf{A}^{\mathrm{T}}(\mathbf{q})$ into the laboratory frame (cf Eq. 19).

$$\mathbf{r}^k_{i,\mathrm{rel}}(t+\Delta t) = \left(\mathsf{A}^k\right)^{\mathrm{T}}\left(\mathbf{q}^k(t+\Delta t)\right)\cdot\boldsymbol{\Delta}^k_i \tag{34}$$

$$\boldsymbol{\omega}^k_{CM}(t+\frac{1}{2}\Delta t) \tag{35}$$

$$\left(\mathsf{A}^k\right)^{\mathrm{T}}\left(\mathbf{q}^k(t+\Delta t)\right)\cdot\boldsymbol{\Omega}^k\left(t+\frac{1}{2}\Delta t\right) \tag{36}$$

With the relative position $\mathbf{r}^k{}_{i,\mathrm{rel}}$ and the angular velocity $\boldsymbol{\omega}^k_{CM}$ in the inertial frame the position and velocities in the inertial frame are updated to

$$\mathbf{r}^k_i(t+\Delta t) = \mathbf{r}^k_{CM}(t+\Delta t) + \mathbf{r}^k_{i,\mathrm{rel}}(t+\Delta t) \tag{37}$$

$$\mathbf{v}^k_i\left(t+\frac{1}{2}\Delta t\right) = \mathbf{v}^k_{CM}\left(t+\frac{1}{2}\Delta t\right) + \omega^k_{CM}\left(t+\frac{1}{2}\Delta t\right) \times \mathbf{r}^k_{i,\mathrm{rel}}(t+\Delta t) \tag{38}$$

References

Abraham FF (1970) Functional dependence of drag coefficient of a sphere on reynolds number. Phys Fluids 13(8):2194

Allen MP, Tildesley DJ (1987) Computer simulation of liquids. Oxford University Press, Oxford

Auroux PA, Iossifidis D, Reyes DR, Manz A (2002) Micro total analysis systems. Part 2. Analytical standard operations and applications. Anal Chem 74(12):2637–2652

Bird RB, Stewart WE, Lightfoot EN (2002) Transport phenomena, 2nd edn. Wiley, New York

Boek ES, Coveney PV, Lekkerkerker HNW, vanderSchoot P (1997) Simulating the rheology of dense colloidal suspensions using dissipative particle dynamics. Phys Rev E 55(3):3124–3133

Chester W, Breach DR, Proudman I (1969) On flow past a sphere at low reynolds number. J Fluid Mech 37:751

Christodoulides N, Tran M, Floriano PN, Rodriguez M, Goodey A, Ali M, Neikirk D, McDevitt JT (2002) A microchip-based multianalyte assay system for the assessment of cardiac risk. Anal Chem 74(13):3030–3036

Clark AT, Lal M, Ruddock JN, Warren PB (2000) Mesoscopic simulation of drops in gravitational and shear fields. Langmuir 16(15):6342–6350

Cundall PA, Strack ODL (1979) A discrete numerical model for granular assemblies. Geotechnique 29(1):47–65

De Fabritiis G, gado-Buscalioni R, Coveney PV (2006) Multiscale modeling of liquids with molecular specificity. Phys Rev Lett 97(13)

Dittrich PS, Schwille P (2003) An integrated microfluidic system for reaction, high-sensitivity detection, and sorting of fluorescent cells and particles. Anal Chem 75(21):5767–5774

Dongarra J, Walker D, Lusk E, Knighten B, Snir M, Geist A, Otto S, Hempel R, Lusk E, Gropp W, Cownie J, Skjellum T, Clarke L, Littlefield R, Sears M, Hussleder man S, Anderson E, Berryman S, Feeney J, Frye D, Hart L, Ho A, Kohl J, Madams P, Mosher C, Pierce P, Schikuta E, Voigt RG, Babb R, Bjornson R, Fernando V, Glendinning I, Haupt T, Ho CTH, Krauss S, Mainwaring A, Nessett D, Ranka S, Singh A, Weeks D, Baron J, Doss N, Fineberg S, Greenberg A, Heller D, Howell G, Leary B, Mcbryan O, Pacheco P, Rigsbee P, Sussman A, Wheat S, Barszcz E, Elster A, Flower J, Harrison R, Henderson T, Kapenga J, Maccabe A, Mckinley P, Palmer H, Robison A, Tomlinson R, Zenith S (1994) Special issue - mpi - a message-passing interface standard. Int J Supercomput Appl High Perform Comput 8(3-4):165

Doyle PS, Bibette J, Bancaud A, Viovy JL (2002) Self-assembled magnetic matrices for dna separation chips. Science 295(5563):2237–2237

Ducrée J, Zengerle R (2004) FlowMap—microfluidics roadmap for the life sciences. Books on demand GmbH, Norderstedt, Germany

Duong TT, Kim G, Ros R, Streek M, Schmid F, Brugger J, Anselmetti D, Ros A (2003) Size-dependent free solution dna electrophoresis in structured microfluidic systems. Microelectron Eng 67-8:905–912

Dupin MM, Halliday I, Care CM (2006) Simulation of a flow focusing device. Phys Rev E 73:055701

Espanol P (1995) Hydrodynamics from dissipative particle dynamics. Phys Rev E 52(2):1734–1742

Espanol P (1998) Fluid particle model. Phys Rev E 57(3):2930–2948

Espanol P, Revenga M (2003) Smoothed dissipative particle dynamics. Phys Rev E 67(2)

Espanol P, Warren PB (1995) Statistical-mechanics of dissipative particle dynamics. Europhys Lett 30(4):191–196

Evans DJ (1977) Representation of orientation space. Mol Phys 34(2):317–325

Evans DJ, Murad S (1977) Singularity free algorithm for molecular-dynamics simulation of rigid polyatomics. Mol Phys 34(2):327–331

Frisch U, Hasslacher B, Pomeau Y (1986) Lattice-gas automata for the navier-stokes equation. Phys Rev Lett 56(14):1505–1508

Glatzel T, Cupelli C, Kuester U, Zengerle R, Santer M (2006a) Aggregating beads in microfluidic chambers on high performance computers compared to experiments. In: 10th anniversary international conference on miniaturized systems for chemistry and life sciences (μTAS), pp 53–55

Glatzel T, Cupelli C, Kuester U, Zengerle R, Santer M (2006b) Simulation of aggregating beads in microfluidics on high performance computers with a fluid particle approach. In: International conference multiscale materials modeling (MMM), pp 54–56

Goldstein H (1980) Classical mechanics, 2nd edn. Addison-Wesley, Reading

Griebel M, Knapek S, Zumbusch G, Caglar A (2004) Numerische Simulationen in der Molekül dynamik. Springer, Berlin

Groot RD, Madden TJ (1998) Dynamic simulation of diblock copolymer microphase separation. J Chem Phys 108(20):8713–8724

Groot RD, Rabone KL (2001) Mesoscopic simulation of cell membrane damage, morphology change and rupture by nonionic surfactants. Biophys J 81(2):725–736

Groot RD, Warren PB (1997) Dissipative particle dynamics: Bridging the gap between atomistic and mesoscopic simulation. J Chem Phys 107(11):4423–4435

Grumann M, Dobmeier M, Schippers P, Brenner T, Kuhn C, Fritsche M, Zengerle R, Ducrée J (2004) Aggregation of bead-monolayers in flat microfluidic chambers simulation by the model of porous media. Lab Chip 4(3):209–213

Grumann M, Geipel A, Riegger L, Zengerle R, Ducrée J (2005) Batch-mode mixing on centrifugal microfluidic platforms. Lab Chip 5(5):560–565

Haeberle S, Zengerle R (2007) Microfluidic platforms for Lab-On-A-Chip applications. Lab Chip 7:1094–1110

Haeberle S, Zengerle R, Ducrée J (2007) Centrifugal generation and manipulation of droplet emulsions. Microfluid Nanofluidics 3:65–75

Hardt S, Schönfeld F (2003) Laminar mixing in different interdigital micromixers. Part II. Numerical simulations. AIChE J 49(3):578–584

Harrison DJ, Wang C, Thibeault P, Ouchen F, Cheng S (2000) The decade's search for the killer ap in μ *tas*. In: Proceedings of the μ *Tas* 2000 Symposium. Kluwer, pp 195–204

Henrich B, Cupelli CG, Moseler M, Santer M (2007) An adhesive dpd wall model for dynamic wetting. Europhys Lett 80:60004

Hessel V, Hardt S, Lowe H, Schonfeld F (2003) Laminar mixing in different interdigital micromixers. Part I. Experimental characterization. AIChE J 49(3):566–577

Heyes DM, Baxter J, Tuzun U, Qin RS (2004) Discrete-element method simulations: from micro to macro scales. Phil Trans R Soc Lond A 362:1853–1865

Hoogerbrugge PJ, Koelman JMVA (1992) Simulating microscopic hydrodynamic phenomena with dissipative particle dynamics. Europhys Lett 19(3):155–160

Johnson RW (1998) The handbook of fluid dynamics. Springer, Heidelberg

Keaveny EE, Pivkin IV, Maxey M, Karniadakis GE (2005) A comparative study between dissipative particle dynamics and molecular dynamics for simple- and complex-geometry flows. J Chem Phys 123(10)

Kerby MB, Spaid M, Wu S, Parce JW, Chien RL (2002) Selective ion extraction: a separation method for microfluidic devices. Anal Chem 74(20):5175–5183

Kim JM, Phillips RJ (2004) Dissipative particle dynamics simulation of flow around spheres and cylinders at finite reynolds numbers. Chem Eng Sci 59(20):4155–4168

Koelman JMVA, Hoogerbrugge PJ (1993) Dynamic simulations of hard-sphere suspensions under steady shear. Europhys Lett 21(3):363–368

Kong B, Yang X (2006) Dissipative particle dynamics simulation of contact angle hysteresis on a patterned solid/air composite surface. Langmuir 22(5):2065–2073

Kurita R, Hayashi K, Fan X, Yamamoto K, Kato T, Niwa O (2002) Microfluidic device integrated with pre-reactor and dual enzyme-modified microelectrodes for monitoring in vivo glucose and lactate. Sens Actuators B Chem 87(2):296–303

Kurita R, Yokota Y, Sato Y, Mizutani F, Niwa O (2006a) On-chip enzyme immunoassay of a cardiac marker using a microfluidic device combined with a portable surface plasmon resonance system. Anal Chem 78(15):5525–5531

Kurita R, Yabumoto N, Niwa O (2006b) Miniaturized one-chip electrochemical sensing device integrated with a dialysis membrane and double thin-layer flow channels for measuring blood samples. Biosens Bioelectron 21(8):1649–1653

Landau LD, Lifshitz EM (2004) Course of theoretical physics. Fluid mechanics, vol 6. Butterworth Heinemann

Lettieri GL, Dodge A, Boer G, de Rooij NF, Verpoorte E (2003) A novel microfluidic concept for bioanalysis using freely moving beads trapped in recirculating flows. Lab Chip 3(1):34–39

Li J, Liao DY, Yip S (1998) Coupling continuum to molecular-dynamics simulation: reflecting particle method and the field estimator. Phys Rev E 57(6):7259–7267

Li PCH, Wang WJ, Parameswaran M (2003) An acoustic wave sensor incorporated with a microfluidic chip for analyzing muscle cell contraction. Analyst 128(3):225–231

Lowe CP (1999) An alternative approach to dissipative particle dynamics. Europhys Lett 47(2):145–151

Luding S (2005) Anisotropy in cohesive, frictional granular media. J Phys Condens Matter 17(24):S2623–S2640

MacDonald MP, Spalding GC, Dholakia K (2003) Microfluidic sorting in an optical lattice. Nature 426(6965):421–424

Marsh CA, Backx G, Ernst MH (1997) Static and dynamic properties of dissipative particle dynamics. Phys Rev E 56(2):1676–1691

Martys NS, Mountain RD (1999) Velocity verlet algorithm for dissipative-particle-dynamics-based models of suspensions. Phys Rev E 59(3):3733–3736

Masters AJ, Warren PB (1999) Kinetic theory for dissipative particle dynamics: the importance of collisions. Europhys Lett 48(1):1–7

Monaghan JJ (1992) Smoothed particle hydrodynamics. Annu Rev Astron Astrophys 30:543–574

Monaghan JJ (2005) Smoothed particle hydrodynamics. Rep Prog Phys 68(8):1703–1759

Nicholson D, Cracknell RF, Quirke N (1995) Direct molecular dynamics simulation of flow down a chemical potential gradient in a slit-shaped micropore. Phys Rev Lett 74(13):2463

Omelyan IP (1998a) On the numerical integration of motion for rigid polyatomics: The modified quaternion approach. Comput Phys 12(1):97–103

Omelyan IP (1998b) Algorithm for numerical integration of the rigid-body equations of motion. Phys Rev E 58(1):1169–1172

Oosterbroek RE, van den Berg A (2003) Lab-on-a-Chip: miniaturized systems for (bio)chemical analysis and synthesis. Elsevier, Amsterdam

Pagonabarraga I, Frenkel D (2001) Dissipative particle dynamics for interacting systems. J Chem Phys 115(11):5015–5026

Peters EAJF (2004) Elimination of time step effects in dpd. Europhys Lett 66(3):311–317

Pivkin IV, Karniadakis GE (2006) Coarse-graining limits in open and wall-bounded dissipative particle dynamics systems. J Chem Phys 124(18)

Proudman I, Pearson JRA (1957) Expansions at small reynolds numbers for the flow past a sphere and a circular cylinder. J Fluid Mech 2(3):237–262

Pryamitsyn V, Ganesan V (2005) A coarse-grained explicit solvent simulation of rheology of colloidal suspensions. J Chem Phys 122(10)

Revenga M, Zuniga I, Espanol P, Pagonabarraga I (1998) Boundary models in dpd. Int J Mod Phys C 9(8):1319–1328

Revenga M, Zuniga I, Espanol P (1999) Boundary conditions in dissipative particle dynamics. Comput Phys Commun 122:309–311

Reyes DR, Iossifidis D, Auroux PA, Manz A (2002) Micro total analysis systems. Part 1. Introduction, theory, and technology. Anal Chem 74(12):2623–2636

Riegger L, Markus Grumann, Nann T, Riegler J, Ehlert O, Mittenbühler K, Urban G, Pastewka L, Brenner T, Zengerle R, Ducree J (2006) Read-out concepts for multiplexed bead-based fluorescence immunoassays on centrifugal microfluidic platforms. Sens Actuators A Phys 126:455–462

Ripoll M, Ernst MH, Espanol P (2001) Large scale and mesoscopic hydrodynamics for dissipative particle dynamics. J Chem Phys 115(15):7271–7284

Roos P, Skinner CD (2003) A two bead immunoassay in a micro fluidic device using a flat laser intensity profile for illumination. Analyst 128(6):527–531

Saleh OA, Sohn LL (2003) Direct detection of antibody-antigen binding using an on-chip artificial pore. Proc Natl Acad Sci USA 100(3):820–824

Sanders JC, Breadmore MC, Kwok YC, Horsman KM, Landers JP (2003) Hydroxypropyl cellulose as an adsorptive coating sieving matrix for dna separations: artificial neural network optimization for microchip analysis. Anal Chem 75(4):986–994

Sato K, Kitamori T (2004) Integration of an immunoassay system into a microchip for high-throughput assay. J Nanosci Nanotechnol 4(6):575–579

Sato K, Yamanaka M, Takahashi H, Tokeshi M, Kimura H, Kitamori T (2002) Microchip-based immunoassay system with branching multichannels for simultaneous determination of interferon-gamma. Electrophoresis 23(5):734–739

Sbragaglia M, Benzi R, Biferale L, Succi S, Sugiyama K, Toschi F (2007) Generalized lattice boltzmann method with multirange pseudopotential. Phys Rev E 75:026702

Sohn YS, Goodey A, Anslyn EV, McDevitt JT, Shear JB, Neikirk DP (2005) A microbead array chemical sensor using capillary-based sample introduction: toward the development of an electronic tongue. Biosens Bioelectron 21(2):303–312

Stone HA, Stroock AD, Ajdari A (2004) Engineering flows in small devices: microfluidics toward a lab-on-a-chip. Annu Rev Fluid Mech 36:381–411

Sugiura S, Oda T, Izumida Y, Aoyagi Y, Satake M, Ochiai A, Ohkohchi N, Nakajima M (2005) Size control of calcium alginate beads containing living cells using micro-nozzle array. Biomaterials 26(16):3327–3331

Sun M, Ebner C (1992) Molecular-dynamics simulation of compressible fluid-flow in 2-dimensional channels. Phys Rev A 46(8):4813–4818

Swope WC, Andersen HC, Berens PH, Wilson KR (1982) A computer-simulation method for the calculation of equilibrium-constants for the formation of physical clusters of molecules—application to small water clusters. J Chem Phys 76(1):637–649

Tabuchi M, Ueda M, Kaji N, Yamasaki Y, Nagasaki Y, Yoshikawa K, Kataoka K, Baba Y (2004) Nanospheres for dna separation chips. Nat Biotechnol 22(3):337–340

Tian HJ, Landers JP (2002) Hydroxyethylcellulose as an effective polymer network for dna analysis in uncoated glass microchips: optimization and application to mutation detection via heteroduplex analysis. Anal Biochem 309(2):212–223

Tian HJ, Huhmer AFR, Landers JP (2000) Evaluation of silica resins for direct and efficient extraction of dna from complex biological matrices in a miniaturized format. Anal Biochem 283(2):175–191

Trofimov SY (2003) Thermodynamic consistency in dissipative particle dynamics, thesis/dissertation. Technische Universiteit Eindhoven, Eindhoven

Vandyke M (1971) Comments on functional dependence of drag coefficient of a sphere on reynolds number. Phys Fluids 14(5):1038–1039

Vattulainen I, Karttunen M, Besold G, Polson JM (2002) Integration schemes for dissipative particle dynamics simulations: from softly interacting systems towards hybrid models. J Chem Phys 116(10):3967–3979

Vilkner T, Janasek D, Manz A (2004) Micro total analysis systems: recent developments. Anal Chem 76(12):3373–3385

Warren PB (2003) Vapor-liquid coexistence in many-body dissipative particle dynamics. Phys Rev E 68(6)

Wolff A, Perch-Nielsen IR, Larsen UD, Friis P, Goranovic G, Poulsen CR, Kutter JP, Telleman P (2003) Integrating advanced functionality in a microfabricated high-throughput fluorescent-activated cell sorter. Lab Chip 3(1):22–27

Yakovleva J, Davidsson R, Lobanova A, Bengtsson M, Eremin S, Laurell T, Emneus J (2002) Microfluidic enzyme immunoassay using silicon microchip with immobilized antibodies and chemiluminescence detection. Anal Chem 74(13):2994–3004

Yakovleva J, Davidsson R, Bengtsson M, Laurell T, Emneus J (2003a) Microfluidic enzyme immunosensors with immobilised protein a and g using chemiluminescence detection. Biosens Bioelectron 19(1):21–34

Yakovleva J, Zherdev AV, Popova VA, Eremin SA, Dzantiev BB (2003b) Production of antibodies and development of enzyme-linked immunosorbent assays for the herbicide butachlor. Analytica Chimica Acta 491(1):1–13

Yoshida M, Tohda K, Gratzl M (2003) Hydrodynamic micromanipulation of individual cells onto patterned attachment sites on biomicroelectromechanical system chips. Anal Chem 75(17):4686–4690